MICROROBOTS

The microDelta: Downscaling robot mechanisms enables ultrafast and high-precision movement

Steven Man[1]†, Sukjun Kim[2,3]†, Sarah Bergbreiter[1,2]*

Physical scaling laws predict that miniaturizing robotic mechanisms should enable exceptional robot performance in metrics such as speed and precision. Although these scaling laws have been explored in a variety of microsystems, the benefits and limitations of downscaling three-dimensional (3D) robotic mechanisms have yet to be assessed because of limitations in microscale 3D manufacturing. In this work, we used the Delta robot as a case study for these scaling laws. We present two sizes of 3D-printed Delta robots, the microDeltas, measuring 1.4 and 0.7 millimeters in height, which demonstrate state-of-the-art performance in both size and speed compared with previously reported Delta robots. Printing with two-photon polymerization and subsequent metallization enabled the miniaturization of these 3D robotic parallel mechanisms integrated with electrostatic actuators for achieving high bandwidths. The smallest microDelta was able to operate at more than 1000 hertz and achieved precisions of less than 1 micrometer by taking advantage of its small size. The microDelta's relatively high output power was demonstrated with the launch of a small projectile, highlighting the utility of miniaturized robotic systems for applications ranging from manufacturing to haptics.

INTRODUCTION

Over the past few decades, advancements in design and manufacturing techniques for small-scale robots, ranging from centimeters to micrometers, have opened up new avenues in scientific research and real-world applications, including micromanipulation (*1*–*3*), microassembly (*2*, *4*, *5*), minimally invasive surgeries (*6*, *7*), and wearable haptic devices providing rich tactile feedback (*8*, *9*). Beyond smaller robots' compact size, scaling laws predict that they can leverage their low mass and high stiffness to achieve superior performance, such as faster movement and higher precision, compared with larger robots (*10*–*13*). The effects of scaling laws have been empirically evaluated by comparing the performances of robots at two different size scales, as demonstrated with centimeter-scale legged robots in (*14*–*17*). However, evaluating the benefits and limitations of scaling laws for robotic mechanisms from the centimeter scale to the millimeter scale remains a challenge.

To manufacture robotic mechanisms at these smaller scales, the convention has been to use two-dimensional (2D) manufacturing methods such as microfabrication and laser machining to create 2D components that are then integrated into 3D robotic mechanisms through postprocessing steps such as manual assembly (*18*–*26*) and folding-based assembly (*3*, *14*–*17*, *27*, *28*). However, the required postprocessing constrains the mechanism design space, creating challenges in further downscaling of robots. In contrast, a 3D-printing process using two-photon polymerization (TPP) with subsequent metallization enables direct writing of complex 3D geometries and actuators without folding or manual assembly. TPP, despite the limited compatible material options, offers a high printing resolution [<100 nm (*29*, *30*)] at a wide range of scales [nano- to mesoscale (*31*)], which makes TPP a promising manufacturing method for microrobots (*32*–*42*). In light of these properties, we envision that TPP can be used to miniaturize robots for superior performance and to study the fundamental advantages and limitations of downscaling in microrobotics.

Here, we present the microDelta robots, some of the smallest and fastest Delta robots to date (Fig. 1). We used a 3D-manufacturing process with TPP previously developed by the authors (*37*, *43*) to downscale the well-known Delta robot, including both actuators and mechanisms, to a base diameter of just 3.2 mm across, before downscaling again to a base diameter of 1.6 mm across. These robots are an order of magnitude smaller than existing parallel robots found in the literature; our smallest Delta robot has a base diameter 9.4 times smaller than the base diameter of the milliDelta robot (*12*) and 13.8 times smaller than the base diameter of the MiGriBot (*4*). The height of the robot results in an even more notable difference. The total height of our smallest Delta robot is only 723 μm, which is 28 times smaller than the milliDelta and about 83 times smaller than the MiGriBot because of the relatively large piezoelectric actuators used in both of these systems.

The small size of the robot in combination with fast electrostatic actuators enables robot actuation at bandwidths greater than 1000 Hz, representing one of the highest bandwidths achieved with any Delta robot mechanism. By leveraging the scalability of the manufacturing method, two versions of microDelta robots were built where one was geometrically scaled by a factor of 2 compared with the other without major changes in the design or manufacturing processes (Fig. 1A). The extensive characterization of both robotic systems illustrates how scaling laws apply in practice and deviate from theoretical predictions because of practical constraints (*10*, *13*, *44*). Last, we demonstrated the microDelta's capability to deliver mechanical work and power to the environment, which are important features for potential practical applications, by launching a projectile into the air.

RESULTS

Design and fabrication of the microDelta robots

As parallel Delta robots, the microDeltas have three legs (3-Revolute-Universal-Universal, 3-RUU) between the ground and the end-

[1]Robotics Institute, Carnegie Mellon University, 5000 Forbes Ave., Pittsburgh, PA 15213, USA. [2]Department of Mechanical Engineering, Carnegie Mellon University, 5000 Forbes Ave., Pittsburgh, PA 15213, USA. [3]Department of Mechanical and Aerospace Engineering, University of California San Diego, 9500 Gilman Drive, La Jolla, CA 92093, USA.
†These authors contributed equally to this work.
*Corresponding author. Email: sbergbre@andrew.cmu.edu

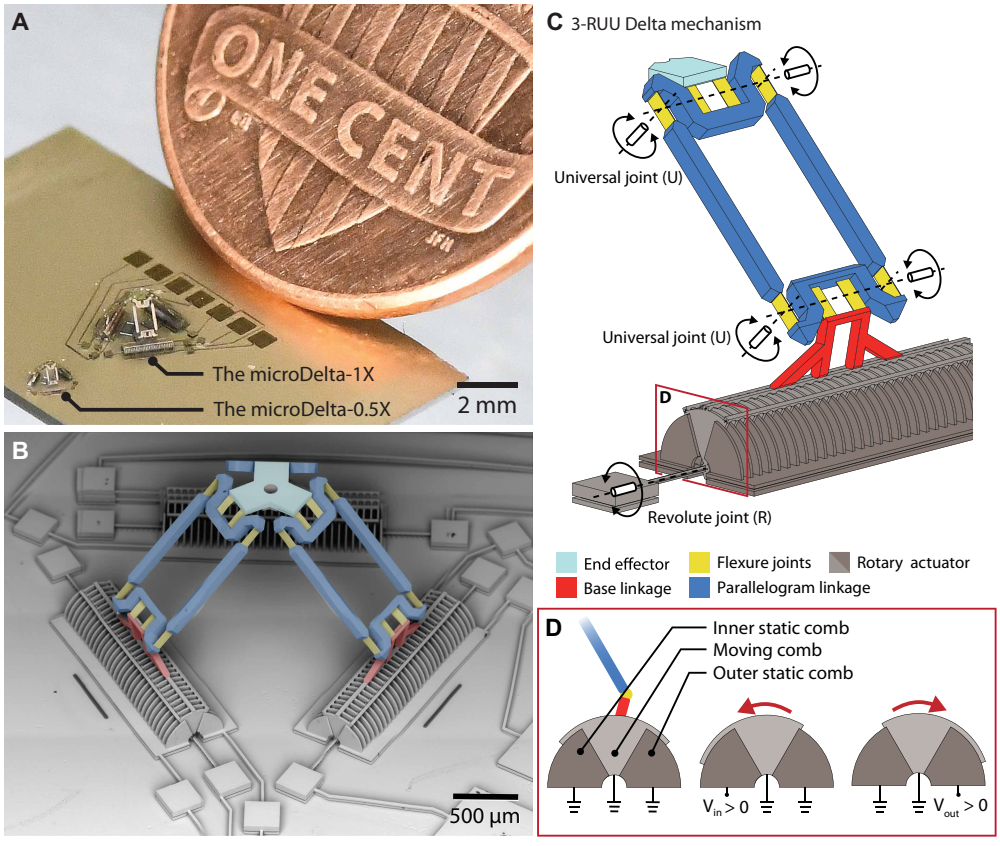

Fig. 1. microDelta robots. (**A**) Two versions of the robot at different size scales are placed next to a US penny. Scale bar, 2 mm. (**B**) Multiple scanning electron microscope images are stitched together to provide a high-resolution image of the microDelta-1X. Scale bar, 500 μm. The linkages and flexures are false-colored to match the schematic in (C). (**C**) Schematic of one leg from the microDelta. Two revolute flexure joints replaced each universal joint. (**D**) Side view of the rotary electrostatic actuator. Two static combs on each side can provide larger angular displacements.

effector planes, which followed the kinematics of conventional Delta robots as shown in Fig. 1 (B and C). Each leg contains a base linkage (red) that pivots at the mechanical ground with a rotary actuator. The base linkage connects to a parallelogram linkage (blue) through one universal joint, and the other end of the parallelogram connects to the end-effector plate (light blue) through the other universal joint (Fig. 1, B and C). Flexure-based compliant joints were used for each joint because they provide beneficial characteristics at the smaller scale, such as zero friction and backlash, compared with pin joints that are conventional at larger scales. The universal joints consist of two revolute flexure joints with their joint axes intersecting each other at a right angle (Fig. 1C). The revolute joints at the base use cross-shaped torsion springs (*45*) to reduce off-axis rotation (fig. S1).

A variation of the 3D electrostatic comb-drive actuators developed by the authors in (*37*) was used to provide rotary inputs to the microDelta robots. The 3D comb-drives are small and fast and can generate pure rotational motions similar to rotary servos at the larger scale, which are all important features to explore downscaling of the Delta robot. This class of electrostatic actuators is also predicted to downscale favorably compared with electromagnetic actuators (*44*, *46*). Two static combs were designed on both sides of the moving comb to provide actuation in both clockwise and counterclockwise directions and to increase workspace (Fig. 1D). The static combs that are closer to the center of the robot's footprint are called "inner static combs," whereas the others are called "outer static combs" for the remainder of this paper. By applying a positive voltage to the inner static comb (V_{in}) while keeping the voltage to the outer static comb (V_{out}) and the moving comb at 0 V (ground), the moving comb rotates inward, and vice versa, as shown in Fig. 1D. The moving comb returns to the center position because of restoring torques from the cross-shaped torsion springs and flexure joints when the applied voltages at the static combs go to zero. Although these electrostatic actuators require a high voltage of up to 200 V, the operating current of the system is typically around 100 nA, so small printed traces and small gauge wires (40 AWG) could easily supply the required voltages. Therefore, compact and lightweight power electronics similar to those developed previously for high-voltage actuators (*47*, *48*) could be positioned farther away from the robot so as not to interfere with the compact robot form factor during operation.

The microDelta robots were manufactured using a process based on 3D printing with TPP previously developed by the authors in (*43*). After printing and release, the surface of the mechanism was metallized to make the 3D-printed structures electrically conductive (Fig. 2, A to C). The detailed fabrication process is described in Materials and Methods. By combining high-resolution 3D structures with 3D-printed actuators in a single process, this approach removed the need for manual assembly. The resulting integration of actuators and complex mechanisms opened access to previously underused design spaces in microrobotic fabrication.

Two sizes of the microDelta robot were designed and fabricated to study how Delta robots scale. The smaller microDelta (microDelta-0.5X) was isometrically scaled down by a factor of 2 when compared with the microDelta-1X (Fig. 1A and fig. S2). The following design modifications were added to microDelta-0.5X because the fabrication of the Delta robot at this smaller scale pushed the limits of the manufacturing process. First, the number of comb-drive fingers (N_f) was reduced, and the finger width of the comb-drive (w_a) was increased to prevent stiction between adjacent comb fingers during fabrication; stiction becomes a more notable issue as the scale decreases (Fig. 2D and the "Scaling of stiction due to capillary force" section in Supplementary Methods). Second, the inner static combs were removed for ease of manufacturing and to improve the fabrication yield. The design parameters of both microDelta robots are described in fig. S1 and tables S1 and S2. Although we have not fabricated a statistically significant number of microDeltas to determine yield (five microDelta-1Xs were fabricated after the design was

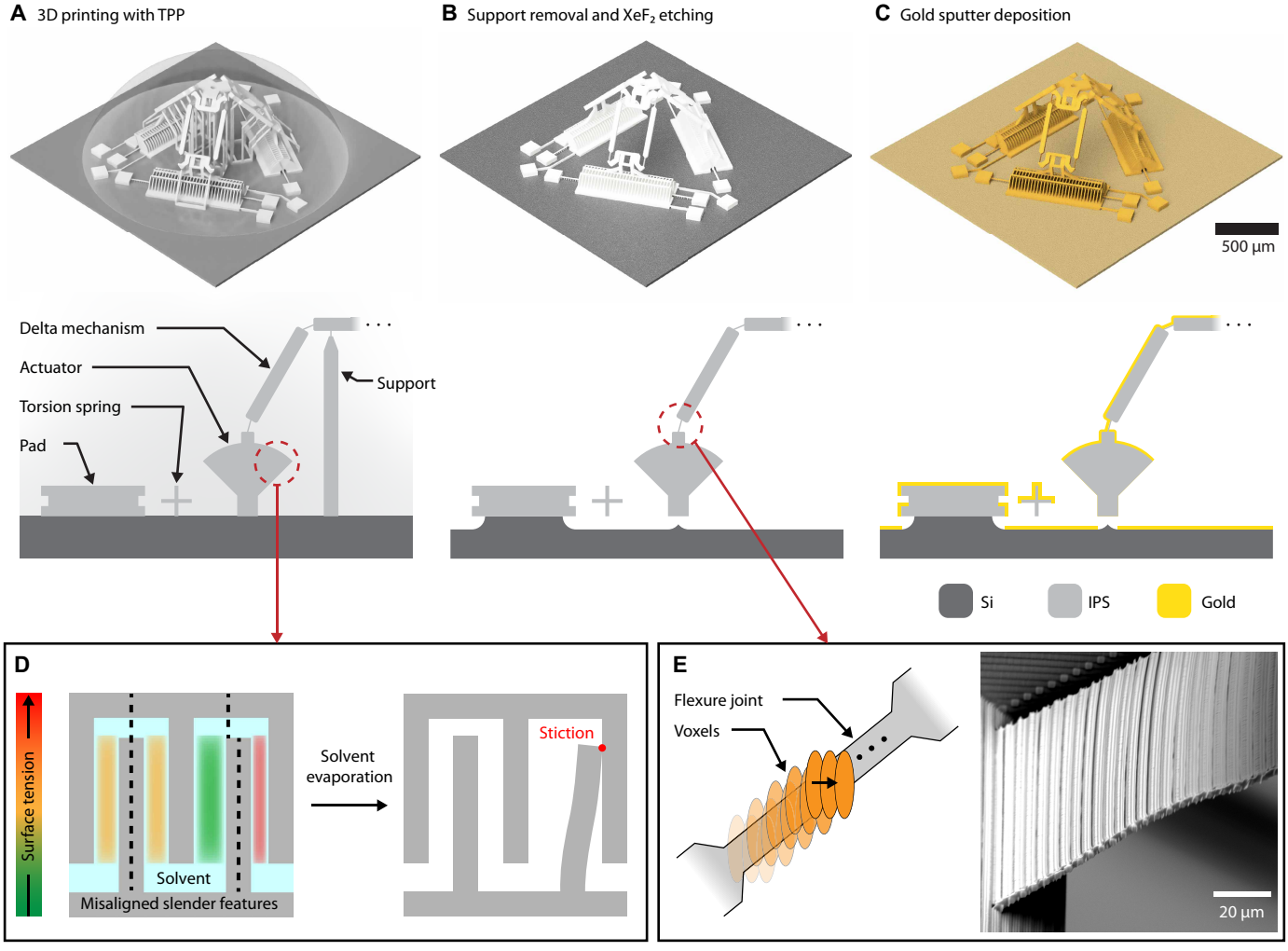

Fig. 2. Fabrication process of the microDelta. (**A**) Desired actuator and mechanism structures are printed on a silicon substrate using TPP. (**B**) The silicon substrate is etched with XeF_2 to release movable structures after development and support removal. (**C**) Gold (50 nm) is sputtered over the entire 3D structure. Scale bar, 500 µm. (**D**) Larger surface tension causes comb finger stiction at small scales. (**E**) The size of the voxel determines the minimum feature size, which affects the thickness of the flexure joints. A close-up scanning electron microscope image of the microDelta's flexure shows the layer lines as a result of the voxel size.

finalized), all of the microDeltas fabricated with the final design parameters were fully functional.

Scaling analysis of the microDelta robots

To analyze the expected performance of the microDelta as it scaled, we needed to calculate how the mechanical and electrical parameters of the robot are affected by a constant scale factor. In this analysis, we assumed that all geometric features—lengths, widths, gaps, and thicknesses—were scaled by an equivalent scaling factor, s. This allowed us to predict both the benefits and limitations of downscaling these robots. A more detailed analysis of scaling is provided in Materials and Methods.

We first explored the scaling of electrostatic torque from the actuators. The electrostatic torque ($\mathbf{T}$) generated by the 3D comb-drives from (*43*) scales as $\mathbf{T} \propto s^1$, implying that actuator torque scales linearly with the geometric scaling variable (s). This analysis assumed that the applied voltage is scale independent, but the maximum voltage that can be applied to an electrostatic actuator is limited by Paschen's curve, which describes the breakdown voltage for various electrode gaps and air pressures (*49*).

The stiffness of both the cross-shaped torsion spring connected to the actuators (k_{cs}) and the stiffness of the flexure joints throughout the mechanism (k_f) will also affect robot metrics like workspace and resonant frequency. In both cases, the stiffness for these flexures scales as k_{cs}, $k_f \propto s^3$. Assuming the linear superposition of torsion stiffnesses, the combined torsional stiffness for the mechanism scales as $k_{tor} = \alpha k_{cs} + \beta k_f \propto s^3$, where α and β are weight coefficients. Therefore, k_{tor} scales much faster than $\mathbf{T}$. The maximum angular displacement of the actuator (θ_{max}) was then calculated by

$$\theta_{max} = \frac{\mathbf{T}}{k_{tor}} \propto s^{-2} \quad (1)$$

which predicts that the actuation angle increases as the scale goes down. Therefore, in the case of perfect isometric scaling, the relative

workspace (workspace normalized by robot volume) of the electrostatically driven Delta robot should increase at smaller scales.

Similarly, we computed an equivalent linear stiffness of the entire microDelta robot (k_{eq}) assuming small displacements

$$k_{eq} = \frac{k_{tor}}{L_c^2} \propto s^1 \quad (2)$$

where L_c is the characteristic length of the microDelta robot legs. Then, the natural frequency of the microDelta robot (f_r) scales as

$$f_r = \sqrt{\frac{k_{eq}}{m_{eq}}} \propto s^{-1} \quad (3)$$

assuming that the equivalent mass of the robot (m_{eq}) scales as s^3. Therefore, the robot bandwidth should increase as the size scale decreases. This higher natural frequency increases the controllable position bandwidth (*50*), allowing smaller robots to complete scaled periodic trajectories with greater speed and accuracy, which can be beneficial for micromanipulation tasks and tremor compensation as presented in (*12*).

We were also interested in how the accuracy of the end-effector position scales. Assuming that the actuators have the same angular displacement resolution ($\Delta\theta_{min}$), the resolution of the end-effector position ($\Delta p_{min} = \Delta\theta_{min} \cdot L_c$) would then scale proportionally with L_c. This scaling ($\Delta p_{min} \propto s^1$) suggested that the root-mean-square (RMS) accuracy of robot trajectory tracking should improve as we shrink the microDelta robot.

Last, at smaller scales, damping and other dissipative forces can become more prominent (*51*). In this work, we considered the scaling of two notable damping mechanisms, material damping and air damping. As the robot moves and flexure joints deform, some of the energy stored in the flexures dissipates because of viscoelasticity in the material. Because the microDeltas were 3D printed with a polymeric material that is known to show viscoelastic behavior (*52*), we modeled the damping coefficient (c_{mat}) as a frequency-dependent dashpot (*14*, *53*). Assuming a scale-independent loss factor for the material, c_{mat} should scale with s^2. In this case, we expect the damping ratio resulting from material damping (ζ_{mat}) to be scale independent,

$$\zeta_{mat} = \frac{c_{mat}}{2\sqrt{m_{eq} k_{eq}}} \propto s^0. \quad (4)$$

In addition, as the robot scales down, viscous air damping can affect robot dynamics because of relatively low Reynolds numbers (*54*, *55*). The Reynolds number of the microDelta-0.5X can be estimated as $Re = 25$ (assuming $L_c = 723$ μm, the robot height, and $v_{max} = \sim 0.5$ m s^{-1}). Among various air damping mechanisms, we hypothesized that the sliding motion between fingers in electrostatic actuators contributes the most viscous damping because of the small gap size ("Scaling of viscous air damping" section in Supplementary Methods). Using the Couette flow model, we found that the torsional damping coefficient of the 3D comb-drive (c_{air}) scales with s^3. Then, the damping ratio of the 3D comb-drive resulting from air damping (ζ_{air}) scales as s^{-1}. Therefore, the damping ratio is expected to increase as the scale decreases, which implies that the effect of viscous air damping becomes more substantial at smaller scales.

Quasistatic characterization

Modeling and calibration

To operate and use the microDelta robots to study practical limitations of downscaling, we built a kinetostatic model to predict the behavior of the robot mechanism given varied voltage inputs. The model calculated the input torques at each actuator as a function of voltage and included link lengths and the stiffnesses of flexure-based joints. We first evaluated the model by characterizing the angular displacement of a single actuator at the base of the microDelta. Modeled displacements toward the inner versus outer combs in fig. S3A are asymmetric because of the asymmetric stiffness of the full microDelta mechanism (fig. S4). The displacements toward both inner and outer static combs were then validated on the fabricated robot up to ±23° (fig. S3, A and B, and movie S1). The experimental results showed a linear relationship between the angular displacement and the squared voltage as expected. A larger discrepancy between the model and experimental results (up to 31.3% at 150 V) was observed when the actuator was moving toward the outer static comb, likely because of variability in comb-drive metallization caused by shadowing from the mechanisms located above the actuators (fig. S5). Similar characterizations were performed on the microDelta-0.5X, which is described in detail in the "Model validation of the microDelta-0.5X" section of Supplementary Methods.

Voltage inputs required for various end-effector trajectories can be calculated using this model, but because of manufacturing variability, discrepancies in actuator performance and joint stiffness between the three legs are inevitable. Therefore, each actuator was calibrated to reduce asymmetries between the legs. To calibrate, the microDelta-1X robot was operated to follow the asterisk trajectories as shown in fig. S6, which involved both inner and outer actuator motions for all three legs. By comparing the length of the line that the robot traveled in all six directions with the desired trajectory length, calibration factors for each static comb were calculated, which were then used to adjust the applied voltages. A detailed calibration procedure is described in Materials and Methods. Figure S6 compares the asterisk trajectory of the microDelta-1X with uncalibrated and calibrated voltages. After calibration, the microDelta-1X was able to follow the asterisk trajectory with an RMS accuracy of 4.6 μm. The same calibration approach was used for both microDelta-1X and microDelta-0.5X; the microDelta-0.5X achieved an RMS accuracy of 0.7 μm for a scaled-down asterisk trajectory.

Trajectory-following characterization

The calibrated microDelta robots were tested to follow various trajectories (a circle, an asterisk, and a star) as shown in Fig. 3 and fig. S7 to evaluate the robot's quasistatic accuracy and precision. For the microDelta-1X, these trajectories spanned ~150 μm by 200 μm on the *xy* plane (Fig. 3, B to D, and movie S2). The *z* height of the commanded trajectories was 1.3 mm, whereas the static equilibrium height (z_{eq}) of the microDelta-1X was 1.4 mm. The trajectories were generated, discretized, and converted into input voltage signals for the actuators using the model. Figure 3A shows the top view of the microDelta-1X's end effector when the robot was actuated to follow the star-shaped trajectory. The recorded positions of the microDelta are plotted in Fig. 3 (B and D), which closely resembled the desired trajectories. The RMS accuracy and precision were calculated and are listed in table S3. The microDelta-1X was able to achieve RMS precisions of 4.6 μm for the asterisk, 3.2 μm for the circle, and 2.1 μm for the star trajectories.

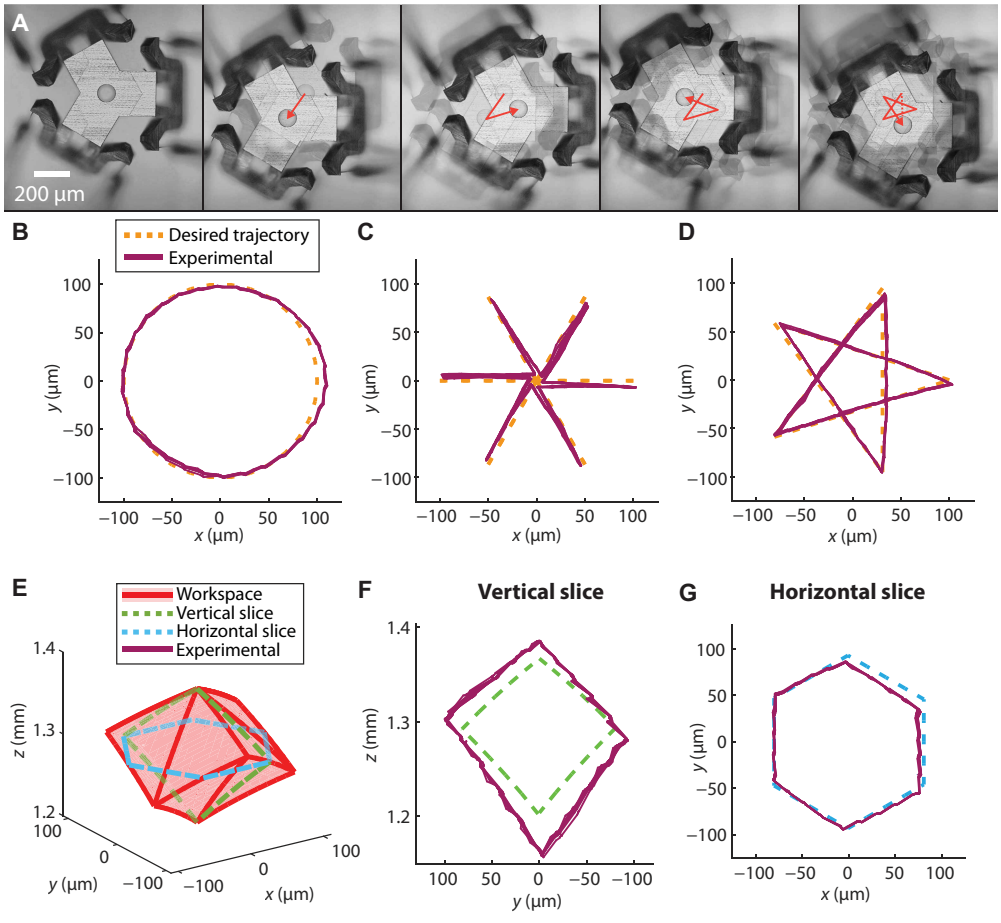

Fig. 3. Quasistatic trajectory-following and workspace characterization results of the microDelta-1X. (**A**) Video stills of the microDelta-1X following the star-shaped trajectory shown from the top view. Scale bar, 200 μm. microDelta-1X following (**B**) circle ($n = 6$), (**C**) asterisk ($n = 6$), and (**D**) star ($n = 6$) trajectories in the *xy* plane. (**E**) Theoretical workspace of the microDelta-1X where horizontal (blue) and vertical slices (green) are followed as trajectories. The theoretical workspace is constructed using sampled points from the microDelta's kinematic model. (**F**) microDelta-1X following a vertical slice (in the *yz* plane) and (**G**) a horizontal slice (in the *xy* plane) of the workspace.

The microDelta-0.5X could also follow the desired trajectories with high precision and accuracy (fig. S7 and movie S3). All trajectories were commanded at a *z* height of 638 μm and scaled down to ~30 μm, except the asterisk trajectory, which was scaled further to 20 μm to reduce the required actuation voltage. The maximum recorded RMS precision error was 0.6 μm (for the asterisk trajectory), and the maximum recorded RMS accuracy error was 1.4 μm (for the circle trajectory) for scaled-down trajectories. However, the relative accuracy errors (RMS accuracy divided by trajectory size) were larger than those of the microDelta-1X. We hypothesize that this discrepancy is due to larger relative manufacturing variability at the smaller scale, causing a larger variation between actuators. This can be further improved as fabrication processes continue to improve in the future.

Workspace characterization

Figure 3E illustrates the 0.0016-mm^3 theoretical workspace of the microDelta-1X, which results from end-effector movement between 150 and 200 μm in the *x*, *y*, and *z* directions. Detailed information on calculation of this workspace is provided in Materials and Methods. The boundaries of two slices from the workspace in the *yz* and *xy* planes were extracted and followed by the robot as shown in Fig. 3 (F and G). The measured workspace boundary in the *xy* plane showed good agreement with the desired trajectory, whereas the results in the *yz* plane showed larger errors in terms of accuracy, which are likely due to a lack of calibration at different *z* heights. The same characterizations were conducted with the microDelta-0.5X, and the results are illustrated in fig. S7. Given that the inner static combs were removed in this robot because of challenges in manufacturing, the reachable workspace of the microDelta-0.5X spanned 20 μm by 30 μm on the *xy* plane.

Frequency response characterization

One of the most substantial advantages of downscaling robotic systems is the high bandwidth achievable because of the high stiffness-to-mass ratio. However, without integrating appropriate actuation methods with scaled mechanisms, previous robots have often struggled to achieve high speed even at small scales (*18*, *22*, *23*). In this work, the 3D printing–based fabrication process enabled the integration of fast 3D electrostatic comb-drive actuators with the Delta mechanism. To characterize the bandwidth of the microDelta robots, the robots were actuated to follow a circular trajectory, and the end effector's movements were recorded at various frequencies using a high-speed camera (Fig. 4, A and B, and movies S4 and S5).

The magnitudes of the mean diameters of the recorded trajectories were then plotted with respect to the frequency as shown in Fig. 4C. For the microDelta-1X, the magnitude decreased as the frequency was increased up to 100 Hz and the plot crossed over the −3-dB line at 20 Hz. The decreasing trend of the magnitude at low frequency (0.2 to 100 Hz) is mainly due to creep in the 3D-printed polymer. The resonance of the microDelta-1X was at 300 Hz, and the recorded shape was highly distorted into an ellipse at this resonant frequency. This elliptical trajectory is a result of one of three actuators becoming dominant in actuation. This was also observed in the modal analysis using finite element analysis software (Ansys 2022R2) (fig. S8 and movie S6). The simulated results showed that the first and second modes of the microDelta-1X both occurred at 305 Hz, which is close to the experimental result. Each mode was dominated by the robot's movement in the direction parallel and normal to one actuator's base revolute joint axis.

For microDelta-0.5X, the peak magnitude was observed at 1050 Hz and only crossed the −3-dB line at 1600 Hz after the resonant peak.

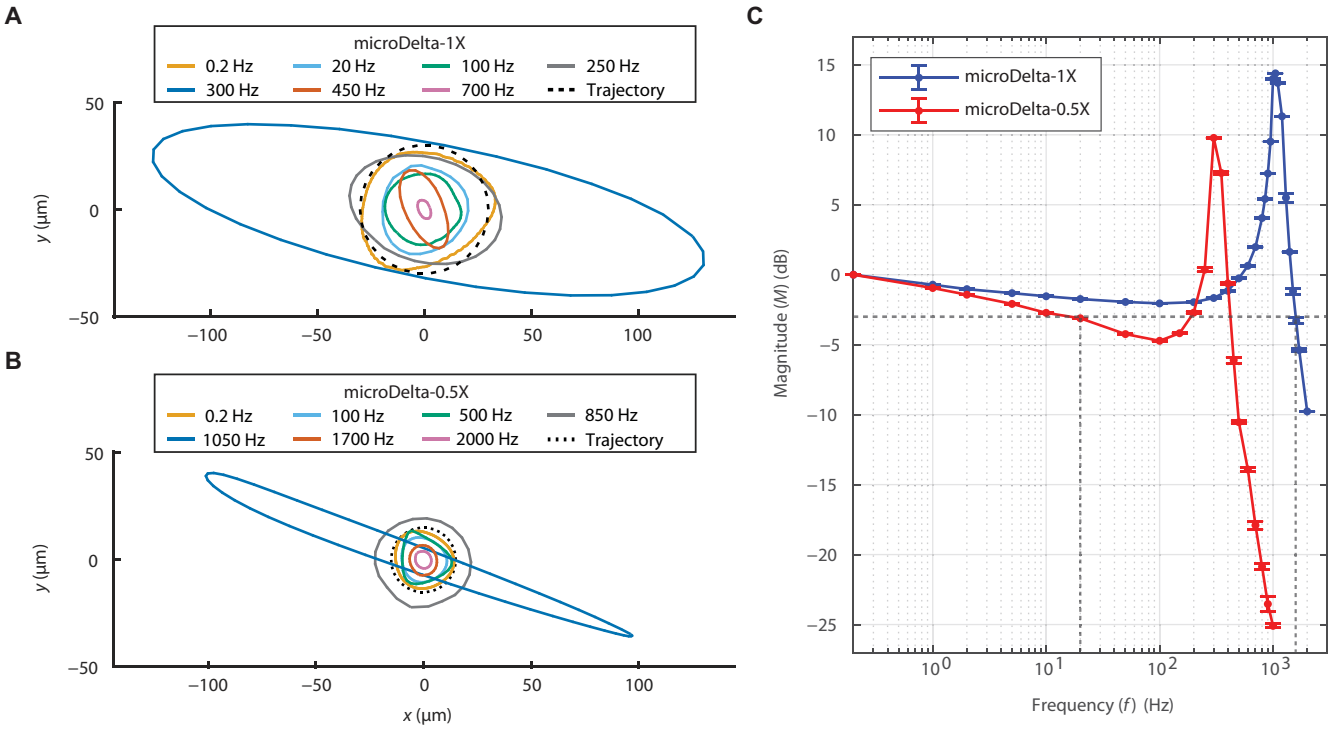

Fig. 4. Frequency response of the microDelta. (**A**) Trajectory of the microDelta-1X at various input frequencies. (**B**) Trajectory of the microDelta-0.5X at various input frequencies. (**C**) Frequency response of the microDelta-1X and microDelta-0.5X. Markers and error bars represent the means and standard deviations, respectively ($n = 3$).

The resonance of the microDelta-0.5X only roughly agreed with the modal analysis result of 877 Hz because the microDelta-0.5X had thicker flexures than designed. The flexure thicknesses were larger than expected because of the minimum voxel height (~3 μm) associated with the current manufacturing process (Fig. 2E). The stiffness of the system was consequently increased, shifting the resonance to a higher frequency than predicted by the designed parameters.

Launching a projectile with the microDelta

The microDeltas' ability to move in 3D space with high precision and speed allows for the potential to address existing challenges in microrobotics, including pick and place of tiny chiplets for microelectronics assembly and vibration isolation for cell manipulation (*12*, *56*–*58*). In addition, the microDeltas can generate high-power actuation by leveraging fast electrostatic actuation combined with the released elastic energy from the flexure joints, thus delivering mechanical work and power to the environment. A sudden energy release from the robot could be used to puncture microscale samples and assist in the release of small objects, which is a substantial challenge in micromanipulation (*59*, *60*). As a demonstration of power delivery, a microscale projectile was launched from the end-effector plate of the microDelta-1X (Fig. 5A and movie S7). A grain of salt with an estimated mass of 37 μg and a 160-μm radius was used as a projectile, which corresponds to the mass of a 400 μm–by–400 μm–by–100 μm silicon chiplet and is ~7.4% of the mass of the robot (500 μg). The dominant adhesion forces between the salt and the microDelta end effector ("Projectile launching power and adhesive forces" section in Supplementary Methods) were expected to be between 2 μN (electrostatic) and 147 μN (capillary, but only if a thin film of water is present) with a gravitational force of only 0.36 μN for the projectile (*59*).

To launch a projectile, the microDelta-1X first slowly lowered the end-effector plate by ramping up the voltage applied to all three outer actuators and loading elastic energy into the flexure joints. The outer voltage was then stepped down to 0 V, while the three inner actuators were actuated with the maximum voltage to quickly raise the end-effector plate and launch the projectile. Taking advantage of both the actuation of the inner combs and the energy release from the springs (flexure joints), the projectile was able to take off from the end-effector plate (Fig. 5B). The video stills of the projectile being launched from the robot are shown in Fig. 5C, and the applied input voltage profiles and projectile movements over time are plotted in Fig. 5 (D and E). The projectile was able to reach a maximum height of 4 mm, which is 12.5 times the diameter of the projectile (320 μm), and was launched from the end-effector plate at $t = 1.4$ ms with an estimated speed of 303 mm s^{-1}. This corresponds to 1.7 nJ of energy transferred from the microDelta to the projectile and an average power of 1.2 μW. Given this average power and the resulting projectile velocity, we estimate that the microDelta exerted an average force of 7.9 μN on the salt grain ("Projectile launching power and adhesive forces" section in Supplementary Methods), enough to overcome typical surface adhesion forces on microscale objects such as microspheres (*59*).

Implications of scaling down

These results demonstrate that downscaling robotic mechanisms can achieve ultrafast and high-precision movement as predicted by scaling laws. The microDelta-0.5X was able to operate at notably high frequencies by leveraging its smaller size. Similarly, the microDelta-0.5X achieved RMS precision errors of ~0.2 μm. However, practical limitations in design and fabrication prevent perfect scaling performance. Table 1 explores these limits by comparing the

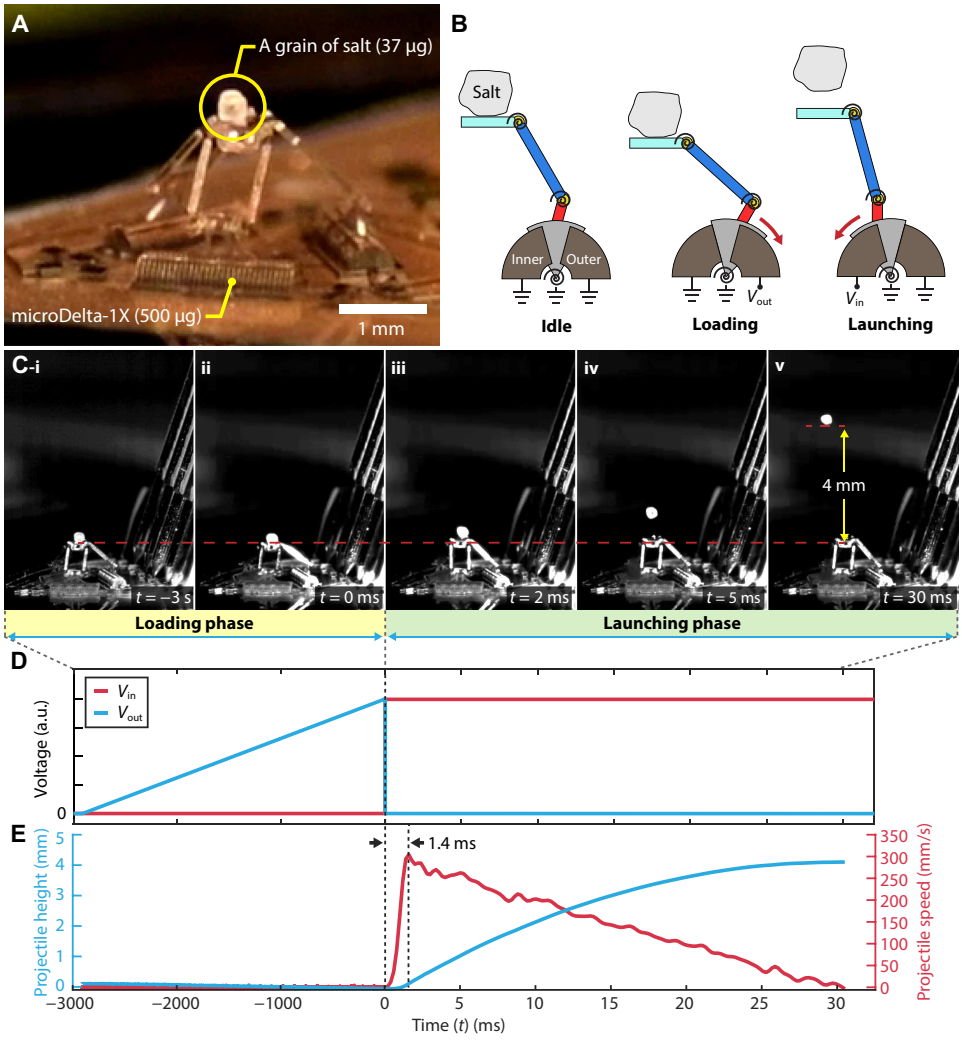

Fig. 5. Projectile launching experiment. (**A**) A grain of salt is placed on the end-effector platform of the microDelta-1X. Scale bar, 1 mm. (**B**) The outer actuators were first actuated to load energy into the torsion springs, and then the inner actuators were actuated to launch the projectile. (**C**) Video stills of the salt-launching experiment ($n = 1$). (**D**) Applied voltage inputs with respect to time. The outer actuator voltage gradually increased during the loading phase and was turned off at $t = 0$ ms. A step voltage input was applied to the inner actuators at $t = 0$ ms. a.u., arbitrary units. (**E**) Projectile height and speed.

normalized torque $\left(\frac{T}{N_f V^2}\right)$, k_{cs}, natural frequency (f_r), θ_{max}, and accuracy (Δp_{min}) of the microDelta-0.5X if everything was perfectly geometrically scaled by half (MD-0.5X theory) versus the microDelta-0.5X as designed in practice (MD-0.5X actual). In this table, a ratio with respect to the microDelta-1X is presented, and numerical values are presented in table S5.

Torque is difficult to measure directly at this scale but can be calculated using the measured dimensions and $\frac{\partial C}{\partial \theta}$ of the actuators. Table 1 identifies a decrease in this torque from what would be expected in an isometrically scaled system because of design concessions like reducing the number of fingers and increasing the finger gap. In addition, the sidewalls of the comb fingers might not have been fully covered with metal during the fabrication process because of smaller gaps between adjacent fingers as characterized in (*61*), which would result in a further decrease in electrostatic torque. The increase in k_{cs} (calculated using the measured spring dimensions) reflects the limitation of the manufacturing resolution of the microDelta flexures, placing a lower bound on flexure thickness and, thus, the stiffness of the system.

From the theoretical scaling analysis, the angular displacement of a single actuator will quadruple if isometrically scaled down by a factor of 2 at the same applied voltage. However, as shown in fig. S9, the outer actuator in the microDelta-0.5X could only generate 5.7° at 100 V, which was smaller than 7.5° generated at the same applied voltage by the microDelta-1X. The discrepancy between the scaling law and the experimental result stems from both the decreased torque and increased flexure stiffness. As a result, the angular displacement of the actuator was reduced, and the relative workspace was decreased more than expected at the smaller scale.

Deviations from isometric scaling can also result in unexpected improvements to metrics. From the scaling analysis, the natural frequency was expected to double as the scale decreased by a factor of 2. However, the measured resonance frequency of the microDelta-0.5X was 3.5 times that of the microDelta-1X. The discrepancy mainly came from the fabrication limits (such as voxel size for flexures; Fig. 2E) along with required design modifications (such as a reduced number of comb fingers), which substantially increased the stiffness and reduced the equivalent mass of the robot. The magnitude of the microDelta-0.5X frequency response results decreased more slowly and did not cross the −3-dB line before 1600 Hz (Fig. 4). The end-effector accuracy of the microDelta-0.5X also exceeded expectations. We hypothesize that this is due to less viscoelastic effect contribution from the 3D-printed polymer, which needs to be studied further.

The effect of viscous air damping on the dynamics of the microDelta robots was minimal. A theoretical damping ratio from air damping in a single 3D comb-drive actuator was only 0.0073 (see the "Scaling of viscous air damping" section in Supplementary Methods for details). Although this damping ratio (ζ_{air}) scales with s^{-1}, the actuator would need to be scaled down more than a factor of 100 to reach a critically damped system. The damping ratio of the entire robot could be higher than that of the actuator because of additional drag on the robot mechanism. However, we found that the microDelta-1X's frequency response in vacuum showed only a slight increase in the magnitude at resonance compared with the response at atmospheric pressure, implying that air damping has a minimal effect on the robot dynamics at these scales ("Frequency response of

Table 1. System characteristics across scales. Metrics of the microDelta-1X (MD-1X), the microDelta-1X theoretically scaled by half, and the microDelta-0.5X. A ratio with respect to the microDelta-1X is presented. Values were calculated or estimated from experimental data except for those with an asterisk (*). Star trajectory results were reported for accuracy (Δp_{min}).

	MD-1X	MD-0.5X theory	MD-0.5X actual	Notes and limitations
$\frac{T}{N_t V^2} = \frac{1}{2N_t}\frac{\partial C}{\partial \theta}$	1	0.5	0.43	Poor metal deposition coverage
k_{cs}	1	0.125	0.32	Flexure thickness below printing resolution
f_r	1*	2	3.5*	Higher stiffness from manufacturing constraints
θ_{max}	1*	4	0.76*	Higher stiffness, reduced number of comb fingers, and increased finger gap size from manufacturing constraints
Δp_{min}	1*	0.5	0.33*	Less viscoelastic polymer

*Values were directly measured.

microDelta-1X under vacuum" section in Supplementary Methods and fig. S10).

We also expanded the scaling analysis to compare several fully implemented parallel robots across three orders of magnitude in characteristic length from our microDelta robots to a meter-scale Delta robot (table S4 and fig. S11). Notably, we found that the bandwidth scales as expected ($\propto s^{-1.03}$), but the accuracy scales slower than expected ($\propto s^{0.54}$), likely because of improved actuator options with a higher angular resolution at larger scales. The volume of the workspace scales much faster than expected ($\propto s^{4.82}$ instead of a naive expectation of s^3), mainly because of larger angular displacements available at the robot base as the scale increases. Detailed comparison and discussion are provided in the "Scaling across several orders of magnitude" section of Supplementary Methods.

DISCUSSION

This work demonstrates some of the smallest and fastest Delta robots by taking advantage of 3D-printed flexure–based mechanisms driven by high-bandwidth electrostatic rotary actuators. Two versions of the robot were designed (microDelta-1X and microDelta-0.5X): The microDelta-0.5X was geometrically scaled down by a factor of 2 compared with the microDelta-1X, with some design modifications as a result of fabrication constraints. The two robots were characterized and compared to study the limits of scaling laws as applied to microrobotic systems. The microDelta-0.5X has a 1.6-mm-diameter footprint and is an order of magnitude smaller than existing Delta robot mechanisms. These miniaturized Delta robots demonstrated translational movements in the 3D space and followed desired trajectories with a minimum RMS accuracy of 0.7 μm for the star and asterisk trajectories and a minimum RMS precision of 0.2 μm for the circle trajectory (table S3) achieved by the microDelta-0.5X. A theoretical workspace volume of 0.0016 mm^3 was achieved with the microDelta-1X, in which the displacement of the end effector spanned between 150 and 200 μm on the x, y, and z axes. By leveraging fast electrostatic actuation with miniaturized mechanisms, the microDelta-0.5X was able to operate at notably high frequencies exceeding its resonance at 1050 Hz. Furthermore, the microDelta robot was able to deliver high power to launch a projectile that weighs 7.4% of the robot's mass to a height of 4 mm with a maximum velocity of 303 mm s^{-1}, which corresponded to about 1.2 μW of average delivered power.

The scaling analysis comparing the microDelta-1X and microDelta-0.5X helps to elucidate the limitations to downscaling that still exist in small-scale robotics and the TPP fabrication process. The main sources of observed discrepancies were related to material and fabrication limitations. The microDelta-0.5X required extremely small features that were close to the printing resolution, and the resulting printed flexures were thicker than designed. In addition, we found that there were more challenges in the design and fabrication of the microDelta-0.5X, such as capillary stiction resulting from compliance from low-modulus printable polymers and smaller gap sizes ("Scaling of stiction due to capillary force" section in Supplementary Methods) as well as poor metallization. These caused further discrepancies between the experimental results and predictions from the scaling analysis for the actuation displacement and workspace. We expect that further improvements to manufacturing processes for small-scale robotic mechanisms, such as more material choices, higher printing resolution, reduced stiction, and improved metallization, will allow us to take advantage of more expected benefits of this downscaling. Further downscaling of the microDelta robots will also need to consider two additional limiting factors of applied voltage and damping given that they affect both the quasi-static and dynamic behaviors of the robots. As the gap between comb-drive fingers reduces, breakdown voltage could also limit the maximum voltage applied to the actuator because of Paschen's curve (*49*). The effect of air damping between the moving and static combs will also increase as these gaps become smaller.

The miniaturized parallel robotic platform in this work can be further optimized for desired tasks, such as micromanipulation, haptic interaction, or releasing microscale samples that often stick to tools. The design parameters for the rotary actuator, flexure joints, and linkage length can be tuned or scaled independently to enhance desired metrics such as bandwidth, accuracy, and workspace. As an example, joint stiffness could be increased in the microDelta mechanism to result in higher bandwidths with the trade-off of workspace. Furthermore, capacitive sensors with the same design as the actuators can be integrated to measure the actuation angle for feedback control of the microDelta robot. This closed-loop control along with the development of dynamic models will simplify the calibration and enable the microDelta to achieve higher accuracy and precision even near the resonant frequency. Then, we can leverage the dynamics of the robot to amplify forces and displacements, ultimately enhancing the efficacy of the robot. A recent parallel micromanipulator

example, the Micro-X4, showed exceptional precision of its end effector (0.35 μm) along with a large workspace of 756 mm^3 in part because of feedback control of the brushless motors used as servo actuators and stiff mechanism design (*3*).

Last, the microDelta robots are very compact when compared with previously developed miniaturized parallel robots, which enables the possibility of densely packed arrays of multiple microDelta robots. These arrays can enable robot manipulation capabilities at small scales that are otherwise impractical. Larger-scale arrays of Delta robots have already been demonstrated for complex manipulation tasks even without added end effectors beyond a static "fingertip" (*62*). These kinds of manipulations are not currently feasible at small scales and could be beneficial for biomedical research or micromanufacturing. In addition, a fingertip-sized Delta robot was previously shown to provide useful haptic feedback (*63*). An array of microDelta robots capable of providing the high-frequency vibrations needed to stimulate certain mechanoreceptors in human skin could ultimately enable rich haptic feedback (*64*). This work provides a quantitative demonstration of scaling laws in Delta robots that can provide a pathway to these future applications.

MATERIALS AND METHODS

Fabrication

The fabrication process used in this work followed similar procedures that were previously developed by authors in (*43*). The microDeltas were 3D printed with a Nanoscribe Photonic Professional GT+ using dip-in laser lithography and a negative photoresist (IP-S, Nanoscribe) on a silicon substrate (Fig. 2A). After the printed structures were developed by propylene glycol methyl ether acetate (Sigma-Aldrich) for 20 min, the sample was immersed in isopropyl alcohol (VWR) for 5 min to remove any excessive photoresist and developer and air dried at room temperature. Support pillars printed under overhanging structures were removed manually with tweezers. The silicon substrate was then dry etched with xenon difluoride (XeF_2) (SPTS Xactix, Xetch) to release the moving combs and the torsional springs (Fig. 2B). Last, 50-nm gold was sputter deposited over the actuator to make the structure electrically conductive (PerkinElmer, 2400-6J) (Fig. 2C).

When designing for fabrication, supports were inserted in the design and manually removed afterward to prevent rigid bodies between flexure joints from drifting apart during printing. The supports were designed to interface with the surfaces of the supported part through a 2-μm-diameter pillar. These supports allowed for removal with minimal damage while remaining capable of resisting drifting. The other design consideration was to ensure the structural stability of high–aspect ratio comb fingers to stiction caused by the surface tension of isopropyl alcohol during drying. Increasing w_a and the gap between two adjacent comb fingers g_a (fig. S1B) prevented such failure modes.

In this work, gold was sputtered over the microDelta actuators instead of the aluminum used in (*43*). To insulate the mechanism from the substrate, we introduced thin gaps that created overhangs like in (*61*) to prevent sputtered metal from fully covering the base of the mechanism. The gap design shown in fig. S1B electrically isolated the actuators from the substrate under a more conformal gold deposition process. The feature has a vertical gap (d) of 10 μm and an overhang of 25 μm. We designed larger pads and traces (Fig. 1A) as part of the 3D-printed structure to implement electrical connections to interface with our custom-designed probing rig as shown in fig. S12.

Scaling analysis

Electrostatic torque

T generated by the 3D comb-drives is modeled in (*43*) as

$$\mathbf{T} = \frac{1}{2}\frac{\partial C}{\partial \theta}V^2 = \frac{1}{2}N_f\epsilon_0\epsilon_r\left(\frac{2R_a t_a - {t_a}^2}{g_a}\right)V^2 \propto s^1 \quad (5)$$

where ϵ_0 is the vacuum permittivity, ϵ_r is the relative permittivity of air, R_a is the outer radius of the comb fingers, and t_a is the thickness of the comb fingers (fig. S1). V is the applied voltage across the actuator and is limited by Paschen's curve (*49*). Breakdown voltage reaches a theoretical minimum with electrode gap spacings of around 5 μm in air at atmospheric pressure. Below 5 μm, the breakdown voltage increases as the gap size decreases. This complex scaling of the breakdown voltage is also affected by the electrode materials, geometries, and surface roughness and would need to be further studied in this specific fabrication process.

Cross-shaped spring stiffness

k_{cs} from (*45*) is

$$k_{cs} = \left(\frac{w_{cs}}{t_{cs}} - 0.373\right)\frac{4Gt_{cs}^4}{3L_{cs}} \propto s^3 \quad (6)$$

where G is the shear modulus and w_{cs}, t_{cs}, and L_{cs} are the width, thickness, and length of the spring, respectively (fig. S1).

Flexure stiffness

k_f can be modeled as in (*65*)

$$k_f = \frac{EI}{L_f} = \frac{Ew_f t_f^3}{12L_f} \propto s^3 \quad (7)$$

where E is the Young's modulus and the subscript f represents the flexure joint dimensions.

Material damping

c_{mat} can be modeled as a frequency-dependent dashpot (*14*, *53*)

$$c_{mat}(f) = \frac{k_{eq}\eta(f)}{2\pi f} \propto \frac{s^1 s^0}{s^{-1}} = s^2 \quad (8)$$

where f is the actuation frequency and $\eta(f)$ is the frequency-dependent loss factor of the material. If we assume that the loss factor is scale independent for simplicity ($\eta \propto s^0$) and the actuation frequency scales as s^{-1} similar to the natural frequency, c_{mat} should scale with s^2. We note that the nonlinear viscoelastic effects and frequency-dependent loss factor will result in a more complex scaling relationship.

Air damping

Detailed modeling of c_{air} (scaling as s^3) is described in the "Scaling of viscous air damping" section of Supplementary Methods and fig. S13. ζ_{air} scales as

$$\zeta_{air} = \frac{c_{air}}{2\sqrt{I_a k_{cs}}} \propto \frac{s^3}{\sqrt{s^5 s^3}} = s^{-1} \quad (9)$$

where I_a is the moment of inertia of the moving comb, which scales with s^5.

Stiction

Scaling also influences our ability to fabricate smaller robots. In addition to more obvious scaling constraints around printing resolution, the gaps in the electrostatic actuators used in the microDelta are subject to stiction when drying. Using a simple model of a cantilever beam separated from a fixed substrate by gap g_b, the beam is constrained to a maximum length (l_{crit}) to avoid stiction (*66*).

$$l_{crit} = \sqrt[4]{\frac{3}{16}\frac{Et_b^3 g_b^2}{\gamma_{la}\cos\theta_c}} \propto s^{\frac{5}{4}} \quad (10)$$

where t_b is the thickness of the beam and γ_{la} and θ_c are the surface tension of the liquid-air interface and contact angle of the drying liquid, respectively. By applying the geometric scaling law, l_{crit} scales with $s^{5/4}$. Therefore, stiction becomes a more critical constraint as the scale decreases ("Scaling of stiction due to capillary force" section in Supplementary Methods).

Quasistatic modeling

The kinematics of Delta mechanisms has been widely studied since their conception. Given conventional Delta robots with pin joints, forward and inverse kinematic solutions from (*67*) would suffice in providing basic insight on how to drive each revolute actuation input at the base. However, the microDelta robots used flexure-based compliant joints, and the resulting nonzero stiffness needed to be considered in the model to understand the robot's behavior. We assumed that flexure joints can provide pure rotation without any shift in the center of rotation, much like the pin joints in conventional Delta robots. The flexure joints were modeled as linear torsional springs using a pseudo–rigid-body model of a small length flexural pivot (*68*).

$$\mathbf{T}_f = k_f \Delta\theta \quad (11)$$

Torque at the flexure joints ($\mathbf{T}_f$) is generated through spring deflection ($\Delta\theta$) with stiffness $k_f = \frac{EI}{L_{h/p}}$, where $I = \frac{w_{h/p}\, t_{h/p}^3}{12}$ and $L_{h/p}$ are the second moment of area and the length of the flexural joints, respectively. The subscript h represents "hinge," referring to flexures that deform along the axis parallel to the cross-spring at the base. The subscript p represents "parallelogram," referring to flexures that compose the parallelogram linkage and rotate about an axis orthogonal to the base cross-spring. $w_{h/p}$ and $t_{h/p}$ can be found in fig. S1 and tables S1 and S2. Young's modulus of the 3D-printed polymer is assumed to be 5.11 GPa (*69*).

We used MATLAB's Simscape Multibody software to model the microDeltas. The 3D–computer-aided design model provided geometric parameters of the mechanism such as linkage length and joint angles. Single–degree-of-freedom revolute joints were positioned at each flexure, where the joint's stiffness was determined by its geometry and verified during actuator and mechanism characterization procedures. Kinematic loop constraints were enforced at the end-effector platform. To calculate the required actuation voltage to the microDelta robots, we used the inverse kinematic equations with the end-effector position as input and obtained the required angular position of the three actuators. We then input those actuator joint angles as constants into the Multibody simulation and solved for actuator torques, which were converted to actuator input voltages using Eq. 5.

Experimental setup

To actuate the microDelta robots, a microcontroller board (Arduino Uno Rev3, Arduino) controlled a digital-analog converter chip (LTC2637, Analog Devices) over the Inter-Integrated Circuit (I^2C) protocol, where the output analog voltages were amplified by a high-voltage amplifier (HV265, Microchip). The amplified voltages were then applied to the actuators by probing the actuator terminals with a custom-made multiprobe needle manipulator (fig. S12) under the probe station (S-250-6, Signatone). The probe needle manipulator is a 3D-printed fixture that holds the spring-loaded needles, which are soldered to wires connected to the output of the amplifier. The trajectories of the microDelta platform were captured using a digital single-lens reflex camera (D850, Nikon) and analyzed with motion analysis software (TEMA T2020, Image Systems). When recording the robot's movement in the *yz* plane, a 45° mirror was used under the probe station. A high-speed camera (Fastcam Mini AX200, Photron) mounted to the probe station was used to capture the frequency response tests, and this camera was used with a microscope lens (K1 CentriMax, Infinity Photo-Optical) to capture the projectile launching test. To analyze the robot's trajectory tracking data, we used the robot's known geometric feature dimensions in the image to find a pixel-to-micrometer ratio, which converted TEMA software's tracking output to displacement in micrometers. The system's measurement uncertainties were ~0.76 and 0.23 μm for the microDelta-1X and microDelta-0.5X, respectively. More information on calculating this measurement uncertainty is provided in the "Statistical analysis" section in Materials and Methods.

Calibration

We calibrated the microDelta robots to mitigate variation in actuator and flexure manufacturing by scaling the actuator voltage input during operation according to the system's uncalibrated trajectory. Using the quasistatic model described above, we first commanded the microDelta to trace an asterisk (fig. S6). This shape consists of strokes that are aligned primarily with only one of the three actuators, which helps to decouple the resultant stiffness caused by multiple sets of actuators and linkages. By comparing the farthest point in each stroke with the desired distance, we obtained a calibration factor $a = \sqrt{l_{desired}/l_{stroke}}$ for our actuator input voltage. Note that the square root in this calibration factor calculation comes from the torque-voltage relationship in Eq. 5. For the microDelta-1X, these empirical calibration factors ranged from 0.78 to 0.95, and for the microDelta-0.5X, they ranged from 1.08 to 1.13.

Workspace characterization

The theoretical workspace was calculated using the robot design parameters and the actuator's range of motion. Although a single actuator had an approximate range of ±20° for the microDelta-1X and 0° to 6° for the microDelta-0.5X as shown in figs. S3A and S9, the actuation ranges used for calculating the theoretical workspace were reduced to ±7.5° for the microDelta-1X and 0° to 3° for the microDelta-0.5X. This was done to avoid robot failure resulting from voltage breakdown during the tests. This workspace constraint ensured that every commanded end-effector position can be reached without any single actuator exceeding the experimental breakdown voltages of 200 V for the microDelta-1X and 120 V for the microDelta-0.5X. Then, we obtained 2D slices in the *xy* and *yz* planes to evaluate the microDelta's ability to follow those trajectories (Fig. 3 and fig. S7).

Frequency response characterization

To capture the frequency response of the microDelta, we used waveform generators (33510B and 33512B, Keysight) to input actuator signals of an approximated circular trajectory at various frequencies and recorded the resulting path using the high-speed camera (Fastcam Mini AX200, Photron). The waveform generators were used instead of the digital-analog converter used in previous experiments to generate outputs at high frequency. Three output channels from the waveform generators were used to actuate three outer actuators. The z height and the radius of the circular trajectory were determined so that only three outer actuators were required to follow the trajectory. Three sinusoidal voltage inputs with 120° phase differences were applied to the actuators to create this circular trajectory. The flexure joint stiffnesses prevented the robot from following a more precise circle shape with these sinusoidal inputs.

At various values of f, the mean radius of the resulting trajectory was calculated as a function of frequency, $R(f)$, to characterize the robot's frequency response

$$R(f) = \frac{1}{N}\sum_{i=1}^{N}\sqrt{{x_i}^2 + {y_i}^2} \tag{12}$$

where x_i and y_i are the i-th end-effector coordinate of N data points in a trial at f. The magnitude (M) was then defined by the following equation

$$M = 20\log\left(\frac{R(f)}{R(0.2\ \text{Hz})}\right) \tag{13}$$

It should be noted that the electrical response time of the circuit was negligible because of the actuator's low capacitance of about 0.42 pF (estimated using a maximum comb finger overlap angle of 17.5°) and resistance of about 4.3 kilohms for the microDelta-1X, resulting in a time constant of ~1.8 ns, a much faster response than the measured bandwidth in the microDelta mechanical system.

Launching experiment

To perform the projectile launching experiment, we loaded a single grain of salt onto the end-effector platform of the microDelta-1X and proceeded to lower the platform by slowly ramping the voltage of the outer comb-drive actuators to their respective maxima. The maximum voltage applied to the actuators varied from 126 to 167 V depending on the calibration factors applied to each actuator. Once the platform was lowered to the absolute minimum of the workspace, all of the inner combs were then instantaneously stepped to the maximum voltage, and the outer combs stepped to 0 V. This actuation profile fully released the stored elastic energy in the flexure joints and launched the projectile using its full actuation power. We recorded the robot and the grain of salt using the high-speed camera (Fastcam Mini AX200, Photron).

Statistical analysis

We calibrated our trajectory measurements to the nominal end-effector size of the microDelta (1X: 520 μm, 488 pixels, 1.07 μm/pixel; 0.5X: 260 μm, 258 pixels, 1.01 μm/pixel). From measurements in the scanning electron microscope, we determined that uncertainty in these printed dimensions (our "ruler") was within 2 μm of our nominal design dimensions (a conservative estimate), resulting in uncertainties of 0.38% and 0.77% for the microDelta-1X and microDelta-0.5X, respectively. For trajectory dimensions of 200 μm in the microDelta-1X, this resulted in a measurement uncertainty from the ruler uncertainty of $\sigma_{\text{ruler,1X}} = 200\ \mu\text{m} \times 0.0038 = 0.76\ \mu\text{m}$ for these trajectories. For trajectory dimensions of 20 and 30 μm, measurement uncertainties from the ruler for the microDelta-0.5X were $\sigma_{\text{ruler,0.5X}} = 0.15\ \mu\text{m}$ and $\sigma_{\text{ruler,0.5X}} = 0.23\ \mu\text{m}$, respectively. We used the larger of the two in our further analysis.

We then determined the uncertainty in our tracking software (TEMA, Image Systems) by recording the motion of both unactuated robots over 2 s to find the standard deviations in pixels ($\sigma_{\text{pixel,1X}} = 0.055$ pixels and $\sigma_{\text{pixel,0.5X}} = 0.025$ pixels), which were then converted to micrometers using the nominal end-effector dimension ($\sigma_{\text{tracking,1X}} = 0.059\ \mu\text{m}$ and $\sigma_{\text{tracking,0.5X}} = 0.025\ \mu\text{m}$).

Next, we calculated a final measurement uncertainty of $\sqrt{\sigma^2_{\text{ruler}} + \sigma^2_{\text{tracking}}}$. This resulted in measurement uncertainties of 0.76 μm and 0.23 μm for the microDelta-1X and microDelta-0.5X, respectively, for trajectory tracking.

Supplementary Materials

The PDF file includes:

Methods
Figs. S1 to S14
Tables S1 to S5
Legends for movies S1 to S7
References (*70*–*73*)

Other Supplementary Material for this manuscript includes the following:

Movies S1 to S7

REFERENCES AND NOTES

1. W. Chen, H. Zhou, B. Zhang, Q. Cao, B. Wang, X. Ma, Recent progress of micro/nanorobots for cell delivery and manipulation. *Adv. Funct. Mater.* **32**, 2110625 (2022).
2. Z. Zhang, X. Wang, J. Liu, C. Dai, Y. Sun, Robotic micromanipulation: Fundamentals and applications. *Annu. Rev. Control Robot. Auton. Syst.* **2**, 181–203 (2019).
3. B. Feng, Y. Liu, J. Zhang, S. Qu, W. Yang, Miniature origami robot for various biological micromanipulations. *Nat. Commun.* **16**, 2633 (2025).
4. M. Leveziel, W. Haouas, G. J. Laurent, M. Gauthier, R. Dahmouche, MiGriBot: A miniature parallel robot with integrated gripping for high-throughput micromanipulation. *Sci. Robot.* **7**, eabn4292 (2022).
5. M. B. Cohn, K. F. Boehringer, J. M. Noworolski, A. Singh, C. G. Keller, K. A. Goldberg, R. T. Howe, "Microassembly technologies for MEMS" in *Microelectronic Structures and MEMS for Optical Processing IV* (SPIE, 1998), pp. 2–16.
6. P. A. York, R. Peña, D. Kent, R. J. Wood, Microrobotic laser steering for minimally invasive surgery. *Sci. Robot.* **6**, eabd5476 (2021).
7. B. J. Nelson, I. K. Kaliakatsos, J. J. Abbott, Microrobots for minimally invasive medicine. *Annu. Rev. Biomed. Eng.* **12**, 55–85 (2010).
8. S. Mintchev, M. Salerno, A. Cherpillod, S. Scaduto, J. Paik, A portable three-degrees-of-freedom force feedback origami robot for human–robot interactions. *Nat. Mach. Int.* **1**, 584–593 (2019).
9. S. B. Schorr, A. M. Okamura, "Fingertip tactile devices for virtual object manipulation and exploration" in *Proceedings of the 2017 CHI Conference on Human Factors in Computing Systems* (ACM, 2017), pp. 3115–3119.
10. W. S. Trimmer, Microrobots and micromechanical systems. *Sens. Actuators* **19**, 267–287 (1989).
11. Z. Liu, W. Zhan, X. Liu, Y. Zhu, M. Qi, J. Leng, L. Wei, S. Han, X. Wu, X. Yan, A wireless controlled robotic insect with ultrafast untethered running speeds. *Nat. Commun.* **15**, 3815 (2024).
12. H. McClintock, F. Z. Temel, N. Doshi, J.-S. Koh, R. J. Wood, The milliDelta: A high-bandwidth, high-precision, millimeter-scale Delta. *Sci. Robot.* **3**, eaar3018 (2018).
13. I. Shimoyama, "Scaling in microrobots" in *Proceedings 1995 IEEE/RSJ International Conference on Intelligent Robots and Systems. Human Robot Interaction and Cooperative Robots* (IEEE, 1995), pp. 208–211.
14. N. Doshi, B. Goldberg, R. Sahai, N. Jafferis, D. Aukes, R. J. Wood, J. A. Paulson, "Model driven design for flexure-based microrobots" in *2015 IEEE/RSJ International Conference on Intelligent Robots and Systems (IROS)* (IEEE, 2015), pp. 4119–4126.

15. K. Jayaram, J. Shum, S. Castellanos, E. F. Helbling, R. J. Wood, "Scaling down an insect-size microrobot, HAMR-VI into HAMR-Jr" in *2020 IEEE International Conference on Robotics and Automation (ICRA)* (IEEE, 2020), pp. 10305–10311.
16. H. Kabutz, K. Jayaram, Design of CLARI: A miniature modular origami passive shape-morphing robot. *Adv. Intell. Syst.* **5**, 2300181 (2023).
17. H. Kabutz, A. Hedrick, W. P. McDonnell, K. Jayaram, "mCLARI: A shape-morphing insect-scale robot capable of omnidirectional terrain-adaptive locomotion in laterally confined spaces" in *2023 IEEE/RSJ International Conference on Intelligent Robots and Systems (IROS)* (IEEE, 2023), pp. 8371–8376.
18. D. S. Contreras, K. S. Pister, "A six-legged MEMS silicon robot using multichip assembly" in *Hilton Head Workshop 2018: A Solid-State Sensors, Actuators and Microsystems Workshop* (Transducer Research Foundation, 2018); 10.31438/trf.hh2018.15.
19. P. E. Kladitis, V. M. Bright, Prototype microrobots for micro-positioning and micro-unmanned vehicles. *Sens. Actuators A* **80**, 132–137 (2000).
20. Q. T. Aten, B. D. Jensen, S. H. Burnett, L. L. Howell, A self-reconfiguring metamorphic nanoinjector for injection into mouse zygotes. *Rev. Sci. Instrum.* **85**, 055005 (2014).
21. K. S. Pister, M. Judy, S. Burgett, R. S. Fearing, Microfabricated hinges. *Sens. Actuators A* **33**, 249–256 (1992).
22. D. Tanaka, Y. Uchiumi, S. Kawamura, M. Takato, K. Saito, F. Uchikoba, Four-leg independent mechanism for MEMS microrobot. *Artif. Life Rob.* **22**, 380–384 (2017).
23. K. Saito, K. Sugita, Y. Ishihara, K. Iwata, Y. Asano, Y. Okane, S. Ono, S. Chiba, M. Takato, F. Uchikoba, Insect-type MEMS microrobot with mountable bare chip IC of artificial neural networks. *Artif. Life Rob.* **22**, 118–124 (2017).
24. Y. Zhu, M. Qi, Z. Liu, J. Huang, D. Huang, X. Yan, L. Lin, A 5-mm untethered crawling robot via self-excited electrostatic vibration. *IEEE Trans. Rob.* **38**, 719–730 (2022).
25. P. Bhushan, C. Tomlin, An insect-scale self-sufficient rolling microrobot. *IEEE Rob. Autom. Lett.* **5**, 167–172 (2020).
26. P. Bhushan, C. Tomlin, Design of an electromagnetic actuator for an insect-scale spinning- wing robot. *IEEE Rob. Autom. Lett.* **5**, 4188–4193 (2020).
27. J. P. Whitney, P. S. Sreetharan, K. Y. Ma, R. J. Wood, Pop-up book MEMS. *J. Micromech. Microeng.* **21**, 115021 (2011).
28. P. S. Sreetharan, J. P. Whitney, M. D. Strauss, R. J. Wood, Monolithic fabrication of millimeter-scale machines. *J. Micromech. Microeng.* **22**, 055027 (2012).
29. S. Maruo, S. Kawata, Two-photon-absorbed near-infrared photopolymerization for three-dimensional microfabrication. *J. Microelectromech. Syst.* **7**, 411–415 (1998).
30. C. N. LaFratta, J. T. Fourkas, T. Baldacchini, R. A. Farrer, Multiphoton fabrication. *Angew. Chem. Int. Ed.* **46**, 6238–6258 (2007).
31. D. E. Marschner, S. Pagliano, P.-H. Huang, F. Niklaus, A methodology for two-photon polymerization micro 3D printing of objects with long overhanging structures. *Addit. Manuf.* **66**, 103474 (2023).
32. G. Adam, A. Benouhiba, K. Rabenorosoa, C. Clévy, D. J. Cappelleri, 4D printing: Enabling technology for microrobotics applications. *Adv. Intell. Syst.* **3**, 2000216 (2021).
33. S. R. Dabbagh, M. R. Sarabi, M. T. Birtek, S. Seyfi, M. Sitti, S. Tasoglu, 3D-printed microrobots from design to translation. *Nat. Commun.* **13**, 5875 (2022).
34. I. Bernardeschi, M. Ilyas, L. Beccai, A review on active 3D microstructures via direct laser lithography. *Adv. Intell. Syst.* **3**, 2100051 (2021).
35. R. S. Pierre, W. Gosrich, S. Bergbreiter, "A 3D-printed 1 mg legged microrobot running at 15 body lengths per second" in *Hilton Head Workshop 2018: A Solid-State Sensors, Actuators and Microsystems Workshop*, vol. 3 (Transucer Research Foundation, 2018); 10.31438/trf.hh2018.16.
36. D. Kim, Z. Hao, J. Ueda, A. Ansari, A 5 mg micro-bristle-bot fabricated by two-photon lithography. *J. Micromech. Microeng.* **29**, 105006 (2019).
37. S. Kim, R. Kubicek, S. Bergbreiter, 3D-Printed electrostatic microactuators for flexible microsystems. *Adv. Funct. Mater.* **33**, 2304991 (2023).
38. L. Ren, N. Nama, J. M. McNeill, F. Soto, Z. Yan, W. Liu, W. Wang, J. Wang, T. E. Mallouk, 3D steerable, acoustically powered microswimmers for single-particle manipulation. *Sci. Adv.* **5**, eaax3084 (2019).
39. F. Qiu, S. Fujita, R. Mhanna, L. Zhang, B. R. Simona, B. J. Nelson, Magnetic helical microswimmers functionalized with lipoplexes for targeted gene delivery. *Adv. Funct. Mater.* **25**, 1666–1671 (2015).
40. I. C. Yasa, H. Ceylan, U. Bozuyuk, A.-M. Wild, M. Sitti, Elucidating the interaction dynamics between microswimmer body and immune system for medical microrobots. *Sci. Rob.* **5**, eaaz3867 (2020).
41. S. Kim, S. Bergbreiter, "3D-printed adaptive microgripper driven by thin-film NiTi actuators" in *2023 IEEE International Conference on Robotics and Automation (ICRA)* (IEEE, 2023), pp. 5445–5451.
42. S. Kim, A. M. Johnson, S. Bergbreiter, Picotaur: A 15 mg hexapedal robot with electrostatically driven, 3D-printed legs. *Adv. Intell. Syst.* **6**, 2400196 (2024).
43. S. Kim, S. Bergbreiter, "Fabrication and characterization of 3D printed out-of-plane torsional comb-drive actuators for microrobotics" in *2021 21st International Conference on Solid-State Sensors, Actuators and Microsystems (Transducers)* (IEEE, 2021), pp. 6–9.
44. G. Caprari, T. Estier, R. Siegwart, "Fascination of down scaling—Alice the sugar cube robot" in *IEEE International Conference on Robotics and Automation (ICRA 2000): Workshop on Mobile Micro-Robots* (IEEE, 2000); 10.3929/ethz-a-010107463.
45. B. P. Trease, Y.-M. Moon, S. Kota, Design of large-displacement compliant joints. *J. Mech. Des.* **127**, 788–798 (2005).
46. P. Chatzakos, E. Papadopoulos, "The influence of dc electric drives on sizing quadruped robots" in *2008 IEEE International Conference on Robotics and Automation* (IEEE, 2008), pp. 793–798.
47. Y. Tang, C. Chen, A. Khaligh, I. Penskiy, S. Bergbreiter, An ultracompact dual-stage converter for driving electrostatic actuators in mobile microrobots. *IEEE Trans. Power Electron.* **29**, 2991–3000 (2014).
48. N. T. Jafferis, E. F. Helbling, M. Karpelson, R. J. Wood, Untethered flight of an insect-sized flapping-wing microscale aerial vehicle. *Nature* **570**, 491–495 (2019).
49. Y. Fu, P. Zhang, J. P. Verboncoeur, X. Wang, Electrical breakdown from macro to micro/nano scales: A tutorial and a review of the state of the art. *Plasma Res. Express* **2**, 013001 (2020).
50. A. Hoevenaars, S. Krut, J. Herder, Jacobian-based natural frequency analysis of parallel manipulators. *Mech. Mach. Theory* **148**, 103775 (2020).
51. R. Lin, W. Wang, Structural dynamics of microsystems—Current state of research and future directions. *Mech. Syst. Signal Process.* **20**, 1015–1043 (2006).
52. N. Rohbeck, R. Ramachandramoorthy, D. Casari, P. Schürch, T. E. Edwards, L. Schilinsky, L. Philippe, J. Schwiedrzik, J. Michler, Effect of high strain rates and temperature on the micromechanical properties of 3D-printed polymer structures made by two-photon lithography. *Mater. Des.* **195**, 108977 (2020).
53. S. H. Crandall, The role of damping in vibration theory. *J. Sound Vib.* **11**, 3–18 (1970).
54. C.-M. Ho, Y.-C. Tai, Micro-electro-mechanical-systems (MEMS) and fluid flows. *Annu. Rev. Fluid Mech.* **30**, 579–612 (1998).
55. Y.-H. Cho, A. P. Pisano, R. T. Howe, Viscous damping model for laterally oscillating microstructures. *J. Microelectromech. Syst.* **3**, 81–87 (1994).
56. D. O. Popa, H. E. Stephanou, Micro and mesoscale robotic assembly. *J. Manuf. Process.* **6**, 52–71 (2004).
57. A. N. Das, P. Zhang, W. H. Lee, D. Popa, H. Stephanou, "μ3: Multiscale, deterministic micro-nano assembly system for construction of on-wafer microrobots" in *Proceedings 2007 IEEE International Conference on Robotics and Automation* (IEEE, 2007), pp. 461–466.
58. D. Chang, G. M. Gu, J. Kim, "Design of a novel tremor suppression device using a linear delta manipulator for micromanipulation" in *2013 IEEE/RSJ International Conference on Intelligent Robots and Systems* (IEEE, 2013), pp. 413–418.
59. B. K. Chen, Y. Zhang, Y. Sun, Active release of microobjects using a MEMS microgripper to overcome adhesion forces. *J. Microelectromech. Syst.* **18**, 652–659 (2009).
60. E. Kim, M. Kojima, K. Kamiyama, M. Horade, Y. Mae, T. Arai, "Accurate releasing of biological cells using two release methods generated by high speed motion of an end effector" in *2016 IEEE/RSJ International Conference on Intelligent Robots and Systems (IROS)* (IEEE, 2016), pp. 2572–2577.
61. S. Kim, C. Velez, R. St. Pierre, G. L. Smith, S. Bergbreiter, A two-step fabrication method for 3D printed microactuators: Characterization and actuated mechanisms. *J. Microelectromech. Syst.* **29**, 544–552 (2020).
62. Z. Si, K. Zhang, O. Kroemer, F. Z. Temel, Deltahands: A synergistic dexterous hand framework based on delta robots. *IEEE Rob. Autom. Lett.* **9**, 1795–1802 (2024).
63. S. B. Schorr, A. M. Okamura, Three-dimensional skin deformation as force substitution: Wearable device design and performance during haptic exploration of virtual environments. *IEEE Trans. Haptics* **10**, 418–430 (2017).
64. J. Yin, R. Hinchet, H. Shea, C. Majidi, Wearable soft technologies for haptic sensing and feedback. *Adv. Funct. Mater.* **31**, 2007428 (2021).
65. L. L. Howell, "Compliant mechanisms" in *21st Century Kinematics: The 2012 NSF Workshop* (Springer, 2013), pp. 189–216; 10.1007/978-1-4471-4510-3_7.
66. N. Tas, T. Sonnenberg, H. Jansen, R. Legtenberg, M. Elwenspoek, Stiction in surface micromachining. *J. Micromech. Microeng.* **6**, 385–397 (1996).
67. R. Williams II, *The Delta Parallel Robot: Kinematics Solutions* (Ohio Univ., 2016); https://people.ohio.edu/williams/html/PDF/DeltaKin.pdf.
68. L. L. Howell, A. Midha, A method for the design of compliant mechanisms with small- length flexural pivots. *J. Mech. Des.* **116**, 280–290 (1994).
69. NanoGuide; https://support.nanoscribe.com/hc/en-gb/articles/360001750353-IP-S.
70. W. Ye, X. Wang, W. Hemmert, D. Freeman, J. White, Air damping in laterally oscillating microresonators: A numerical and experimental study. *J. Microelectromech. Syst.* **12**, 557–566 (2003).
71. R. L. Flemmer, C. Banks, On the drag coefficient of a sphere. *Powder Technol.* **48**, 217–221 (1986).
72. Pocket Delta Robot (Asyril SA); https://onexia.com/wp-content/uploads/2023/10/ONExia-Asyril-Delta.pdf.
73. IRB 360 FlexPicker (ABB); https://search.abb.com/library/Download.aspx?DocumentID=ROB0082EN_G.

Acknowledgments: We thank Z. Temel for insightful conversations that inspired the initial idea for this work. We also thank the staff of the Claire & John Bertucci Nanotechnology Laboratory and the Soft Lithography Lab at Carnegie Mellon University for assistance in microfabrication and 3D printing. **Funding:** This work was supported in part by a Carnegie Mellon Manufacturing Futures Initiative seed grant, in part by the Presidential Fellowship from Carnegie Mellon University, in part by the Robotics Institute Summer Scholars program, and in part by the National Science Foundation under grant CMMI-2408884. **Author contributions:** Conceptualization: S.K. and S.B. Methodology: S.K. and S.B. Software: S.M. Validation: S.M. and S.K. Formal analysis: S.M., S.K., and S.B. Investigation: S.M. and S.K. Data curation: S.M. Writing—original draft: S.M., S.K., and S.B. Writing—review and editing: S.M., S.K., and S.B. Visualization: S.M. and S.K. Supervision: S.B. Project administration: S.B. Funding acquisition: S.M., S.K., and S.B. **Competing interests:** The authors declare that they have no competing interests. **Data and materials availability:** The data for this study have been deposited in the Dryad repository at doi.org/10.5061/dryad.7pvmcvf56.

Submitted 21 March 2025
Accepted 14 October 2025
Published 12 November 2025
10.1126/scirobotics.adx3883

Science Robotics

The microDelta: Downscaling robot mechanisms enables ultrafast and high-precision movement

Steven Man, Sukjun Kim, and Sarah Bergbreiter

Sci. Robot. **10** (108), eadx3883. DOI: 10.1126/scirobotics.adx3883

Science Robotics (ISSN 2470-9476) is published by the American Association for the Advancement of Science. 1200 New York Avenue NW, Washington, DC 20005. The title *Science Robotics* is a registered trademark of AAAS.